Journal of Materials Chemistry C

The Unique Luminescent Properties and Enhanced Thermal Stability of A Novel All-Inorganic Perovskite CsCaCl3:Mn2+ for Solid-state Lighting Application

Journal:	*Journal of Materials Chemistry C*
Manuscript ID	TC-ART-11-2023-004189.R1
Article Type:	Paper
Date Submitted by the Author:	04-Dec-2023
Complete List of Authors:	Liu, Zhichao; Wenzhou University Ding, Yihong; Wenzhou University, College of Chemistry and Materials Engineering Fu, XiaoXiao; Wenzhou University Pan, Yuexiao; Wenzhou University, Li, Liyi ; Sun Yat-Sen University

ARTICLE

The Unique Luminescent Properties and Enhanced Thermal Stability of A Novel All-Inorganic Perovskite $CsCaCl_3:Mn^{2+}$ for Solid-state Lighting Application

Received 00th January 20xx,
Accepted 00th January 20xx

DOI: 10.1039/x0xx00000x

Zhichao Liu [a], Yuexiao Pan [a,]*, Xiaoxiao Fu [a], Yihong Ding [a], Liyi Li [b,]*

The development of efficient, non-toxic, and cost-effective white-light emitters is crucial for advancing lighting technology. Here, we present a groundbreaking study on a new all-inorganic perovskite crystal, $CsCaCl_3:Mn^{2+}$, which exhibits temperature sensing and hue-tunable white light emission. The $CsCaCl_3$ matrix emits broad blue light at 455 nm due to self-trapped excitons (STEs) emission. Upon Mn^{2+} doping, the $CsCaCl_3:Mn^{2+}$ crystal emits broad yellow light at 555 nm, originating from the Mn^{2+} $^4T_1(G)$ - $^6A_1(S)$ transition. Increasing Mn^{2+} concentration led to a decrease in blue emission intensity, accompanied by enhanced yellow emission, suggesting an energy transfer from STEs to Mn^{2+}. The enhanced stability of $CsCaCl_3:Mn^{2+}$ compared to pure $CsCaCl_3$ is demonstrated through thermal analysis. The distinctive temperature-dependent responses of STEs and Mn^{2+} emissions in $CsCaCl_3:Mn^{2+}$ suggest its potential application in temperature sensing. The synthesis process for this luminescent crystal is both straightforward and scalable, making it a promising candidate for large-scale applications.

Introduction

Inorganic luminescent crystals have garnered significant attention in recent years due to their remarkable optoelectronic properties and potential applications in lighting and display technologies. [1-5] In particular, the inorganic perovskite luminescent materials have sparked widespread interest due to its unique properties such as high photoluminescence efficiency, tunable bandgap, and excellent charge transport characteristics.[3-5] However, there is a crucial need to explore new materials that are non-toxic and abundant, considering the environmental and health concerns associated with the commonly used toxic lead (Pb) and cadmium (Cd) containing materials.[6-20] This has motivated researchers to investigate alternative materials that offer both efficient luminescence and reduced toxicity.

One of the coveted goals in the field of luminescent materials is the realization of single-component white light emission. Past research endeavors have explored the incorporation of multiple ions into host matrices to generate diverse emissions that can be mixed to achieve white light.[20-22] By employing a co-doping strategy involving Sn^{2+} and Mn^{2+}, the activation of cyan-orange dual-band emission with complementary spectral ranges is achieved, originating from the self-trapped excitons and d-d transitions of Sn^{2+} and Mn^{2+} centers, respectively, within the Rb_4CdCl_6 host. Interestingly, efficient Mn^{2+} emission is achieved through ultra-efficient energy transfer between Sn^{2+} and Mn^{2+} facilitated by the formation of adjacent exchange-coupled Sn-Mn pairs, despite the inherent challenges in exciting Mn^{2+} ions doped in Rb_4CdCl_6.[20] A white light composed of two tunable broadband emissions with a standout color-rendering index (CRI) of 94 for the fabricated white-light emitting diode (WLED) has been yielded by co-doping Bi^{3+} and Te^{4+} in Cs_2SnCl_6.[21] A single-component white light-emitting Mn^{2+}-doped perovskite colloidal $CsPbCl_3$ Quantum Dots. show pure white light emission with a commission International d'Eclairage (CIE) coordinate value of (0.31, 0.33) and a high photoluminescence (PL) yield of 66%.[22] However, such approaches often involve the introduction of multiple ions, leading to increased complexity, cost, and toxicity concerns. Therefore, the development of a simple and effective strategy to obtain single-component white light emission remains a significant challenge.

The hexagonal $CsCdCl_3$ perovskites, subject to doping with Sb^{3+}/Mn^{2+}, demonstrate a vivid red/orange afterglow emission post UV excitation removal. The exhibited phenomena reveal an extended duration of luminescence, presenting prospective applications spanning from biological imaging, and photodynamic therapy, to optical

[a]*Key Laboratory of Carbon Materials of Zhejiang Province, College of Chemistry and Materials Engineering, Wenzhou University, Wenzhou 325035, P.R. China. E-mail: yxpan@wzu.edu.cn; Fax&Tel: +86-577-88373017*

[b]*School of Chemical Engineering and Technology, Sun Yat-sen University, Zhuhai 519082, P. R. China.*
E-mail: lily255@mail.sysu.edu.cn
Electronic Supplementary Information (ESI) available: [details of any supplementary information available should be included here]. See DOI: 10.1039/x0xx00000x

anti-counterfeiting measures.[23,24] We believe that $CsCaCl_3$ will exhibit similar properties to $CsCdCl_3$ due to both compounds belong to the perovskite family and share a cubic crystal structure with Cs^+ cations occupying the *A*-site and Cd^{2+} or Ca^{2+} cations occupying the *B*-site. This structural similarity leads to comparable bonding environments and lattice arrangements within the two materials. Furthermore, the ionic radii of Cd^{2+} and Ca^{2+} ions are relatively close, resulting in similar interatomic distances and bonding characteristics in $CsCaCl_3$ and $CsCdCl_3$. The similar chemical environments provided by the central metal cations contribute to analogous electronic and optical properties in terms of luminescence, absorption, and other relevant characteristics. However, no luminescence has been reported for $CsCaCl_3$. Therefore, the host matrix $CsCaCl_3$ emerges as a promising candidate due to its inherent structural and optical properties. Its low toxicity, abundance, and ease of synthesis make it an intriguing host material for luminescent applications.

In this study, we present an investigation into the luminescent properties of Mn^{2+}-doped $CsCaCl_3$ crystals, unveiling their potential for single-component white light emission. Through the investigation of the luminescent characteristics of $CsCaCl_3$:Mn^{2+}crystals, our objective is to make a meaningful contribution to the ongoing pursuit of environmentally friendly and effective lighting solutions, while simultaneously addressing the existing challenges within this domain.

Experimental

2.1. *Synthesis of $CsCaCl_3$:Mn^{2+} Crystals*

$CsCaCl_3$:Mn^{2+} crystals were synthesized via a hydrothermal method using high-purity raw materials. CsCl (99.9%), $CaCl_2$ (99.9%), $MnCl_2$ (99.9%), and hydrochloric acid HCl (36.5 wt%) were purchased from Aladdin Chemistry Co., Ltd (China). The synthesis process involved the following steps: 1 mmol CsCl, 1-*x* mmol $CaCl_2$, and *x* mmol $MnCl_2$ (*x* varied between 0% and 8%) were mixed with 3 mL HCl in a 15 mL Teflon liner. The resulting solution was subjected to hydrothermal treatment at 160 °C for 12 hours. After completion, the autoclave was slowly cooled to room temperature. The obtained crystals were separated from the supernatant solution by centrifugation. Subsequently, the crystals were washed three times with ethyl alcohol and dried at 60 °C for 12 hours.

2.2. *Characterization Methods*

The synthesized $CsCaCl_3$:Mn^{2+} crystals were subjected to comprehensive characterization to assess their structural and optical properties. X-ray powder diffraction (XRD) patterns were recorded on a Bruker D8 Advance XRD using Cu Kα radiation (λ = 0.15418 nm) at a scan rate of 10° min^{-1} within the range of 10-60°. The PL properties were characterized using a FluoroMAX-4-TCSPC fluorescence spectrophotometer, equipped with a 450 W xenon arc lamp and a photomultiplier tube, covering a measurement range of 200-900 nm. To investigate the excitation and emission spectra, the crystals were excited with appropriate wavelengths, and the resulting luminescence emission was recorded. The UV-vis diffuse reflectance spectra (DRS) were measured on a UV-visible diffuse reflectance spectrometer (SolidSpec-3600) with $BaSO_4$ as a reference material. The chemical composition on the surface of the particles was analyzed using x-ray photoelectron spectra (XPS) on an ESCALAB 250Xi versa probe spectrometer, with Al *Kα* radiation (h*ν* = 486.6 eV) as the monochromatic source.

2.3. *Fabrication of WLEDs*

To evaluate the practical application of $CsCaCl_3$:Mn^{2+} crystals as white-light emitters, the as-synthesized $CsCaCl_3$:*x*Mn^{2+} (*x* = 0.8%, 1%, 2%) crystals were fabricated on the 310 nm InGaN LED chip. The crystals were thoroughly mixed with epoxy resin and coated on semiconductor LED chips, respectively. Subsequently, the devices were solidified at 130 °C for 1 hour to produce solid-state WLEDs. The photoelectric properties of the WLEDs were measured using an integrating sphere spectro-radiometer system (HAAS-1200, Everfine).

2.4. *Computational Methodology*

Density functional theory (DFT) calculations were conducted employing the Vienna Ab initio Simulation Package (VASP). To expand electronic wave functions, a plane-wave basis with a cutoff energy of 350 eV was employed, and the Brillouin zone was sampled using a Γ-only k-mesh. The $CsCaCl_3$ system was constructed using a supercell with dimensions of 3 × 3 × 2, comprising 60 atoms. Furthermore, the $CsCaCl_3$:Mn^{2+} system was configured by substituting one Ca atom with a Mn atom, resulting in a Mn^{2+} doping concentration of 8.0 mol%. The exchange-correlation interactions were described using the Generalized Gradient Approximation (GGA) with the Perdew-Burke-Ernzerhof (PBE) function. Electron-ion interactions were represented using projector-augmented wave (PAW) pseudopotentials.[25] Spin-polarized DFT calculations have been performed via PBE+U, and the Coulomb U and exchange J parameters ((Ueff = U - J = 5.94) have been employed.[18]

Results and discussions

3.1. *Structures, PL Properties, and Electronic Band Structures of $CsCaCl_3$ and $CsCaCl_3$:Mn^{2+} Crystals.*

In **Fig. 1**, we present a comprehensive investigation of the structural and compositional modifications in the $CsCaCl_3$ lattice upon the introduction of Mn^{2+}. The schematic representation of the modified structures is shown in **Fig. 1**a. The crystal structure of $CsCaCl_3$ presents a characteristic three-dimensional (3D) crystal structure with a cubic $Pm\bar{3}m$ symmetry, resembling that of $CsPbBr_3$.[27] In this structure, the $[CaCl_6]^{4-}$ octahedra are completely isolated by Cs^+ ions. The substitution is performed on an equimolar basis, and the lattice parameters and coordination environment of Mn^{2+} are following those of Ca^{2+}. The substituting Ca^{2+} ions with Mn^{2+} ions result in the formation of $[MnCl_6]^{4-}$ octahedral structures and induces a structural modification. The XRD patterns of $CsCaCl_3$ and $CsCaCl_3$:Mn^{2+} matched with the pure $CsCaCl_3$

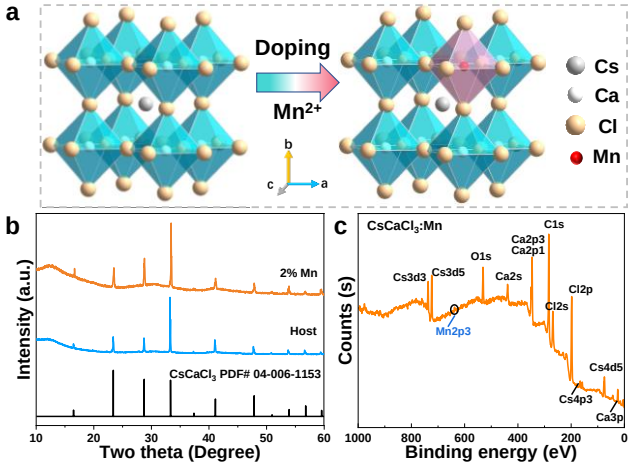

Fig. 1 (a) Schematic representation of the structures modified by introducing Mn^{2+} into the $CsCaCl_3$ lattice. (b) XRD patterns $CsCaCl_3$ and $CsCaCl_3$:Mn^{2+}. (c) XPS spectra of $CsCaCl_3$:Mn^{2+}.

phase, as confirmed by the standard card PDF#04-006-153 (**Fig. 1**b). As depicted in **Fig. S1**, the obtained profile factors in Rietveld refinement plots are R_{wp} = 6.05 and R_p= 3.79% for $CsCaCl_3$, and R_{wp} = 6.34 and R_p= 4.30% for $CsCaCl_3$:Mn^{2+}, respectively. The results reveal the good fitting quality and confirm the successful synthesis of desirable pure phases. However, a noticeable shift towards higher diffraction angles was observed in $CsCaCl_3$:Mn^{2+} compared to $CsCaCl_3$. This shift can be attributed to the smaller ionic radius of Mn^{2+} (80 pm) compared to Ca^{2+} (99 pm), which results in a slight compression of the crystal lattice.

XPS spectra of $CsCaCl_3$:Mn^{2+} confirm the composition of the sample (**Fig. 1**c). Clear peaks corresponding to the elements Cs, Ca, Cl, and Mn are observed, indicating the successful incorporation of Mn^{2+} into the $CsCaCl_3$ lattice. In **Fig. S2**, the high-resolution XPS analysis of the $CsCaCl_3$:Mn^{2+} sample reveals detailed information regarding the elemental composition, chemical states, and binding energies of Cs, Ca, Cl, and Mn. The results demonstrate the successful modification of $CsCaCl_3$ by introducing Mn^{2+} ions, leading to structural changes and the presence of Mn in the lattice.

In **Fig. 2**, we investigated the PL properties of $CsCaCl_3$:$x$$Mn^{2+}$ (x = 0% - 5%). Under visible light, both $CsCaCl_3$ and $CsCaCl_3$:$x$$Mn^{2+}$ with different Mn^{2+} concentrations appeared as colorless and transparent crystals (**Fig. 2**a). However, under 314 nm UV light excitation, an intriguing luminescent behavior is observed. Pure $CsCaCl_3$ emits blue light, while the emission from $CsCaCl_3$:$x$$Mn^{2+}$ evolves from blue to yellow as the Mn^{2+} concentration increases from 0% to 5%, passing through intermediate cold, neutral, and warm white light hues. This phenomenon underscores that the introduction of Mn^{2+} into the host $CsCaCl_3$ matrix can efficiently yield a broad range of white light with varying color temperatures.

Excitation spectra were monitored at 454 nm (**Fig. 2**b) and 555 nm (**Fig. 2**c), respectively, to investigate the origin of the excitation light. The excitation signal observed at 454 nm was predominantly associated with the self-trapped excitons (STEs) within the $CsCaCl_3$ matrix. In contrast, the excitation at 555 nm closely resembled the behavior at 454 nm, suggesting that the luminescence at 555 nm from Mn^{2+} ions is likely stemming from STEs-mediated energy transfer mechanisms, rather than arising from d-d transitions of Mn^{2+} ions transition from the $^4T_1$(G) state to the $^6A_1$(S) state (**Fig. S3**).

The excitation spectra of $CsCaCl_3$:$x$$Mn^{2+}$, as monitored at 454 nm, exhibit a noteworthy behavior, with the most intense peak observed at a 1% Mn^{2+} concentration. As the concentration of Mn^{2+} increases, the intensity of this peak gradually diminishes. This observation suggests the potential occurrence of energy transfer processes from STEs to Mn^{2+}. The decreasing intensity with higher Mn^{2+} concentrations is indicative of the greater efficiency of this energy transfer mechanism. Conversely, the excitation spectra of $CsCaCl_3$:$x$$Mn^{2+}$ at 555 nm exhibit contrasting trends emerge. Here, as the Mn^{2+} concentration increases from 0 to 5%, the excitation intensities successively rise and then decrease with the Mn^{2+} concentration further increased to 8%. This phenomenon can be attributed to the concentration quenching effect, wherein increased Mn^{2+} concentrations promote non-radiative processes that deactivate the luminescent centers, leading to a decrease in the luminescence efficiency. Under 314 nm excitation, the emission spectrum primarily consists of two distinct bands located at 454 nm and 555 nm, attributed to transitions originating from STEs and Mn^{2+} $^4T_1$(G) - $^6A_1$(S), as depicted in **Fig. 2**d.[19,25,28] The intensity changes of the excitation spectra at 454 nm and 555 nm corresponded well with the intensity changes of the emission spectra at 454 nm and 555 nm, respectively.

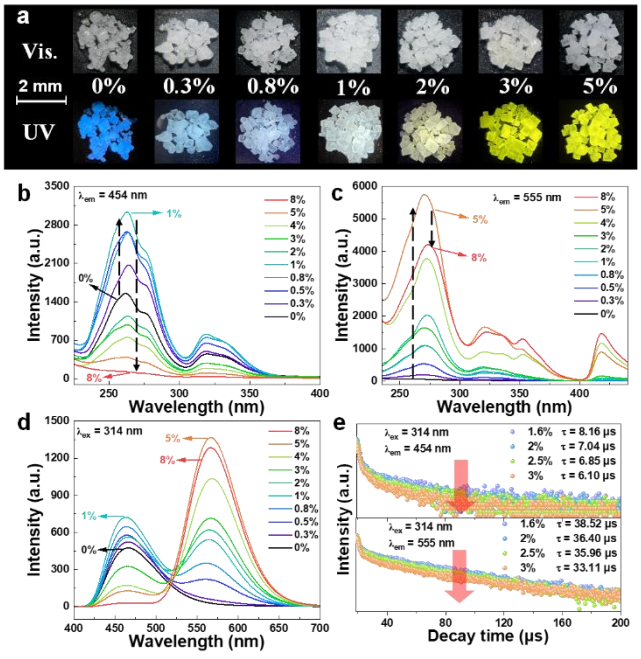

Fig. 2 (a) Photographs of $CsCaCl_3$:$x$$Mn^{2+}$ (x = 0% - 5%) under visible and 314 nm UV lights. Excitation spectra of $CsCaCl_3$:$x$$Mn^{2+}$ were monitored at (b) 454 nm and (c) 555 nm. (d) Emission spectra of $CsCaCl_3$:$x$$Mn^{2+}$ varied with x value. (e) PL decay curves of emission at 454 and 555 nm in $CsCaCl_3$:$x$$Mn^{2+}$.

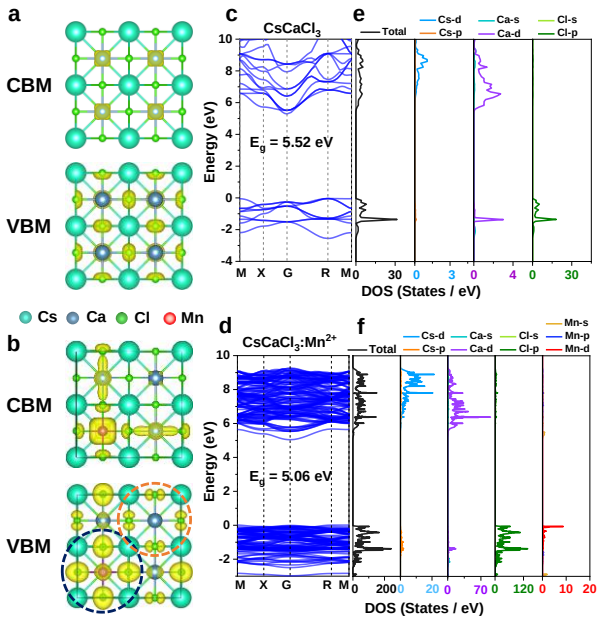

Fig. 3 (a,b) Charge density distribution of the conduction band minimum (CBM) and the valence band maximum (VBM), and (c,d) calculated electronic band structure and (e,f) density of states of (a,c,e) $CsCaCl_3$ and (b,d,f) $CsCaCl_3$:Mn^{2+} crystals.

Therefore, it can be concluded that the blue light from the STEs of $CsCaCl_3$ matrix and the yellow light from Mn^{2+} complement each other to produce white light. The chromaticity coordinates diagram of $CsCaCl_3$:$x$$Mn^{2+}$ (x = 0%, 0.8%, 1%, 1.6%, 2%, and 5%) reveals a transition from blue light towards white light and subsequently to yellow light as the Mn^{2+} doping concentration increases. This shift in chromaticity coordinates indicates the tunability of the emitted light color in $CsCaCl_3$:$x$$Mn^{2+}$ phosphors through controlled Mn^{2+} doping, which is essential for various optoelectronic applications (**Fig. S4**). The emission spectra of $CsCaCl_3$:$x$$Mn^{2+}$ under excitation at 275 nm displayed an analogous variation pattern to that observed under 314 nm excitation (**Fig. S5**). This consistency implies that the emission characteristics of $CsCaCl_3$:$x$$Mn^{2+}$ are independent of the excitation wavelength, suggesting the absence of any significant influence of excitation energy on the Mn^{2+} emission behavior within the host lattice. This also suggests that the emission mechanism is likely due to energy transfer from the host lattice to the Mn^{2+} ions, rather than direct excitation of the Mn^{2+} ions themselves.

Notably, the presence of absorption peaks for Mn^{2+} in the range of 400-500 nm suggests its capability to absorb a portion of the blue light emitted by $CsCaCl_3$, providing a theoretical basis for the energy transfer from $CsCaCl_3$ to Mn^{2+}. Furthermore, it is observed that with increasing Mn^{2+} concentration from 1% to 5%, the blue emission from the $CsCaCl_3$ matrix weakens, while the yellow emission from Mn^{2+} intensifies. In the meantime, the PL lifetime of Mn^{2+} emissions at 555 nm decreases from 38.52 to 33.11 μs as the concentration of Mn^{2+} ion increases from 1.6 to 3 mol%, providing further evidence for efficient energy transfer processes from STEs to Mn^{2+} ions ($ET_{STEs \rightarrow Mn}$) (**Fig. 3e**). In addition, the efficiency (η_T) of the energy transfer from STEs to Mn^{2+} ions can be obtained using the equation below:[26]

$$\eta_{\tau_{ET}} = 1 - \tau_s / \tau_{s0} \quad (1)$$

where τ_S and τ_{S0} are the lifetimes of the STEs in the presence and absence of Mn^{2+} ions, respectively. Therefore, the energy transfer efficiency which is calculated by the lifetimes ($\eta_{\tau_{ET}}$) from STEs to Mn^{2+} gradually increases from 28.55% to 56.82%, along with the concentration of Mn^{2+} ions increasing in $CsCaCl_3$:Mn^{2+} (**Fig.** S6).

The charge density distribution of the conduction band minimum (CBM) and the valence band maximum (VBM) in $CsCaCl_3$ and $CsCaCl_3$:Mn^{2+} crystals were investigated in **Fig. 3**. The electronic band structure and density of states were calculated to further understand the effect of Mn^{2+} doping on the electronic properties of $CsCaCl_3$. The introduction of Mn^{2+} dopants resulted in a slight reduction in the band gap from 5.52 eV to 5.06 eV. The yellow emission observed can be attributed to d-d transitions of Mn^{2+} ions. The charge density of $CsCaCl_3$:Mn^{2+} was mainly distributed on Mn and nearby Cl ions, while Cl ions far away from Mn^{2+} contributed very little to the charge distribution (black circle). On the other hand, in $CsCaCl_3$ crystals, the electron distribution was primarily located on Cl ions adjacent to Ca (pink circle). Therefore, it can be

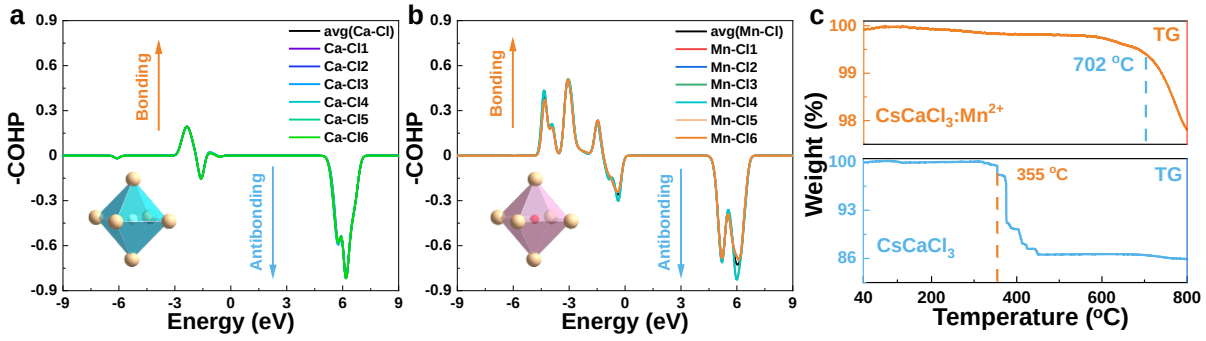

Fig. 4 Crystal orbital Hamiltonian populations (-COHP) of (a) Ca-Cl bonds in $CsCaCl_3$ and (b) Mn-Cl bonds in $CsCaCl_3$:Mn^{2+}. TG and DTA curves of (c) $CsCaCl_3$ and $CsCaCl_3$:Mn^{2+} were measured using thermal gravimetric analysis (TGA/SDTA851, Switzerland) from room temperature to 800 °C at a heating rate of 10 °C min^{-1}.

inferred that the localized charge distribution of Mn^{2+} and the different electron distributions in $CsCaCl_3$:Mn^{2+} and $CsCaCl_3$ crystals suggest that the emission processes of Mn^{2+} and STEs may compete with each other. The shift in the band gap and the selective charge distribution within the crystal lattice provide valuable insights into the intricate photoluminescent behavior of $CsCaCl_3$:Mn^{2+} and further our understanding of its potential for optoelectronic applications.

3.2. *Enhanced Thermal Stability and Unique Temperature Response of $CsCaCl_3$:Mn^{2+}*

The crystal orbital Hamiltonian populations (-COHP) calculation is a method used to analyze the bonding interactions between atoms in a crystal structure.[18] It provides valuable insights into the nature and strength of chemical bonds. In this study, the -COHP analysis was performed on the Ca-Cl and Mn-Cl bonds in $CsCaCl_3$ and $CsCaCl_3$:Mn^{2+}. The -COHP values for Ca-Cl and Mn-Cl bonds are found to be -0.7455 eV and -0.91815 eV, respectively. These values indicate the average energy associated with the bonds. When Mn is introduced into $CsCaCl_3$, there is a notable increase in the average -COHP for Mn-Cl bonds compared to Ca-Cl bonds. The more negative the icohp value, the stronger the covalent bond between the corresponding atoms. Therefore, the calculated icohp values suggest that both Ca-Cl and Mn-Cl bonds exhibit significant covalent character in $CsCaCl_3$ and $CsCaCl_3$:Mn^{2+}. The enhancement in thermal stability upon Mn doping is further corroborated by the thermogravimetric (TG) and differential thermal analysis (DTA) curves, as shown in **Fig. 4c.** The data reveal that $CsCaCl_3$ begins to decompose at 355 °C, whereas $CsCaCl_3$:Mn^{2+} exhibits a significantly higher thermal stability, decomposing only at 702 °C. This substantial increase in thermal stability can be attributed to the stronger Mn-Cl bonding introduced by the Mn doping.

The improved thermal stability can be explained by the higher energy associated with Mn-Cl bonds, as indicated by the more negative -COHP values. These stronger bonds make it energetically less favorable for the crystal structure to undergo decomposition at elevated temperatures. Consequently, the strengthened bonding interactions resulting from the doping of Mn^{2+} ions contribute to the increased thermal stability observed in $CsCaCl_3$:Mn^{2+}. This observation is of significant importance for potential applications in high-temperature environments or materials where enhanced thermal stability is desired.

The temperature-dependent PL emission spectra of $CsCaCl_3$ show a gradual decrease in the intensity of the STEs emission and a noticeable blue shift in the emission peak as the temperature is increased from 313 K to 473 K (**Fig. S7**). This behavior can be attributed to thermal activation processes that result in decreased trapping of charge carriers by defects and enhanced mobility within the crystal lattice, leading to the observed reduction in STEs emission intensity and the blue shift. Upon cooling from 473 K to 313 K, the intensity returns to approximately 98% of the initial value, and the emission wavelength reverts to its original position, indicating the reversible nature of these thermal effects. In $CsCaCl_3$:2%Mn^{2+}, the emission intensity of both the STEs and Mn^{2+} decreases with increasing temperature (**Fig. S8**). The Mn^{2+} emission experiences a blue shift during heating and returns to its initial position during cooling, with the intensity largely recovering to its initial value. This behavior is attributed to the variation in the electron-phonon coupling and the crystal field surrounding the Mn^{2+} ions, demonstrating the ability of $CsCaCl_3$:Mn^{2+} to withstand temperature-induced alterations while maintaining its emission properties.

The Debye temperature (θ_D) serves as a valuable parameter for characterizing structural flexibility and lattice vibrational behavior. Its determination is achievable through the utilization of the following computational expressions: [18,29,30]

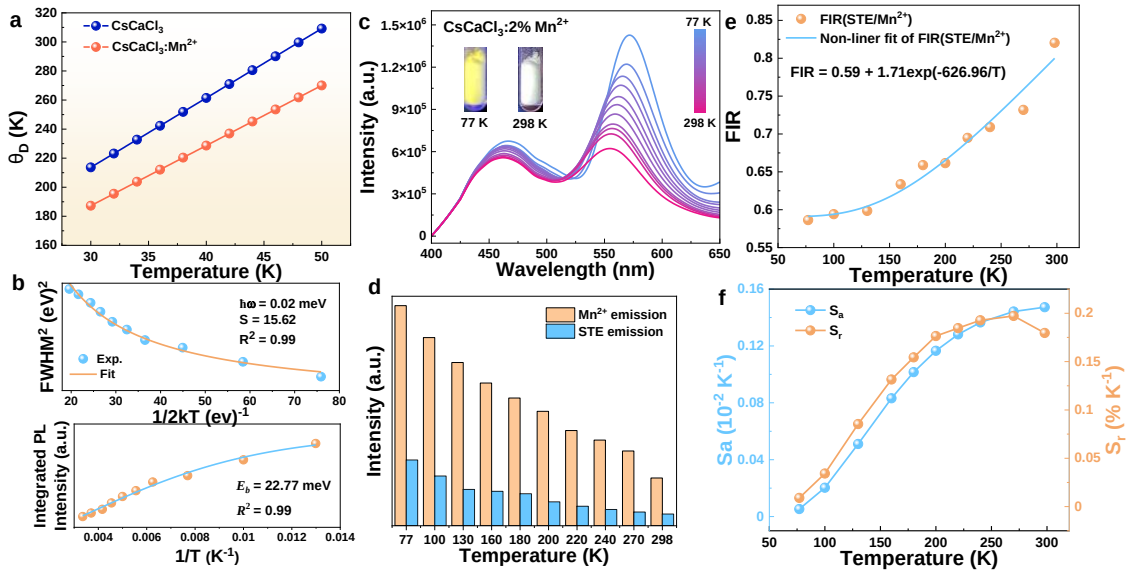

Fig. 5 (a) Debye temperature tested from 30 to 50 K for $CsCaCl_3$ and $CsCaCl_3$:Mn^{2+}. (b) Temperature-dependent FWHM (upper) and integrated PL intensity (bottom) of the fitting curves of STE emission. (c) Emission spectra and (d) the integrated intensity of STE and Mn^{2+} emission dependent on the temperature (inset: photos of $CsCaCl_3$:Mn^{2+} measured at 77 and 298 K under excitation of 314 nm). (e) Fitting curve of temperature-dependent FIR (STE/Mn^{2+}). (f) Absolute sensitivity (S_a) and relative sensitivity (S_r) versus absolute temperature for $CsCaCl_3$:Mn^{2+} under 314 nm excitation.

$$v_s = \sqrt{\frac{G_x}{\rho}};\ v_p = \sqrt{\frac{Bx + \frac{4Gx}{3}}{\rho}};\ v_m = \frac{\frac{2}{v_s^3} + \frac{1}{v_p^3}}{3} \quad (2)$$

$$\theta_D = \frac{h}{k} v_m \left(\frac{3nN_A\rho}{4\pi M}\right)^{\frac{1}{3}} \quad (3)$$

where h and k_B represent the reduced Plank constant and Boltzmann constant, respectively. The Avogadro constant, N_A is employed along with the molecular weight, M, and the material density, ρ.

The θ_D can be extracted from DFT computations by analyzing the bulk and shear moduli, as well as wave velocities, including v_s (shear wave velocity), v_p (longitudinal wave velocity), and v_m (average wave velocity). In our investigations, the calculated θ_D for $CsCaCl_3$ is determined to be 233.7 K, while for $CsCaCl_3$:Mn^{2+}, it amounts to 227.7 K (**Fig. 5**a). Notably, the calculated Debye temperature of $CsCaCl_3$ is generally lower than that of most other perovskite materials (**Table S1**). This suggests that the structural lattice of $CsCaCl_3$ is relatively soft, which may lead to the formation of STE emission. Moreover, doping with Mn^{2+} further reduces the θ_D value, indicating that the introduction of Mn^{2+} leads to a softer lattice structure in $CsCaCl_3$.

To gain deeper insights into the influence of electron-phonon coupling on the spectral characteristics of $CsCaCl_3$:Mn^{2+}, the temperature-dependent emission band broadening of STEs is analyzed using the following equation:[31]

$$FWHM(T) = 2.36\hbar\omega_{phonon}\sqrt{S\coth\left(\frac{\hbar\omega_{phonon}}{2kT}\right)} \quad (4)$$

where S is Huang-Rhys factor, $\hbar\omega_{phonon}$ is the phonon frequency, and k is the Boltzmann constant. A high, albeit appropriate, S value within the range of 10 to 40 indicates the facile formation of STEs, leading to robust STEs emission.[29,32,33] In the case of $CsCaCl_3$:Mn^{2+}, the calculated S value for STEs is 15.62 (as shown in **Fig. 5**b), underscoring the strong electron-phonon coupling attributed to the Jahn-Teller effect. Additionally, it is noteworthy that the exciton binding energy (E_b) can be estimated using the activation energy in the Arrhenius formula, as denoted by equation (3):[29]

$$I(t) = I_0 / (1 + Ae^{-E_b/kT}) \quad (5)$$

where I_0 is the intensity of 0 K E_b is the exciton activation energy, and k is the Boltzmann constant. The E_b value of STEs emission is 22.77 meV, closely resembling the room-temperature thermal energy (~25 meV), affirming the stable existence of STEs in $CsCaCl_3$.

To delve further into the properties of the blue STEs and yellow Mn^{2+} emissions in $CsCaCl_3$:Mn^{2+}, temperature-dependent PL spectra are measured across a temperature range of 77-298 K under 314 nm excitation, as depicted in **Fig. 5**c. It is observed that the Mn^{2+} emissions at 555 nm exhibit rapid degradation as the temperature increases from 77 to 298 K, while the intensity of STEs emissions retains 82.1% of its initial value. Notably, Mn^{2+} emissions experience a blueshift of approximately 15 nm, attributable to the intensified electron-phonon coupling effect and associated lattice deformation at elevated temperatures. Furthermore, **Fig. 5**d presents the integral intensity of Ca^{2+} STEs and Mn^{2+} emissions at different temperatures, highlighting the differential sensitivity of STEs and Mn^{2+} emissions to temperature.

This distinct behavior leads to the exploration of $CsCaCl_3$:Mn^{2+} nanocrystals for optical thermometry. To this end, the fluorescence intensity ratio (*FIR*) technique is employed to establish a correlation between temperature and *FIR*, as elucidated by the equations: [34,35]

$$FIR = \frac{I_{STE}}{I_{Mn}} = \frac{I_{0,STE}}{I_{0,Mn}} \frac{1 + A_{Mn}\exp(-\Delta E_{Mn}/k_BT)}{1 + A_{STE}\exp(-\Delta E_{STE}/k_BT)} \approx B + C\exp(-\Delta E/k_BT) \quad (6)$$

The constants B, C, and ΔE are associated with Ca^{2+} and Mn^{2+} ions. As illustrated in **Fig. 5**e, the *FIR* values increase from 0.59 to 0.82 as the temperature ranges from 77 K to 298 K. In the field of temperature sensing, the absolute temperature sensitivity (S_a) and relative temperature sensitivity (S_r) are crucial parameters to assess the quality of optical thermometry, and they can be computed using the expressions:[36]

$$S_a = \left|\frac{\partial FIR}{\partial T}\right| = C\exp(-\Delta E/k_BT)\frac{\Delta E}{k_BT^2} \quad (7)$$

$$S_r = \left|\frac{1}{FIR}\frac{\partial FIR}{\partial T}\right| = \frac{C\exp\left(\frac{-\Delta E}{k_BT}\right)}{B + C\exp\left(\frac{-\Delta E}{k_BT}\right)}\frac{\Delta E}{k_BT^2} \quad (8)$$

The calculated S_a and S_r values are depicted in **Fig. 5**f, with the maximum values reaching as high as 0.0014 and 0.20% K^{-1}, respectively. Furthermore, temperature resolution (δ_T) is an important parameter for evaluating the performance of optical thermometry, expressed as follows:[37]

$$\delta_T = \frac{1}{S_r}\frac{\Delta FIR}{FIR} \quad (9)$$

In this context, $\Delta FIR/FIR$ represents the relative error in the measurement process, which is estimated to be approximately 0.5%.[38] Accordingly, the minimum temperature resolution at 298 K is calculated to be 2.5 K. These findings highlight the potential of $CsCaCl_3$:Mn^{2+} nanocrystals as promising materials for noncontact optical thermometry applications.

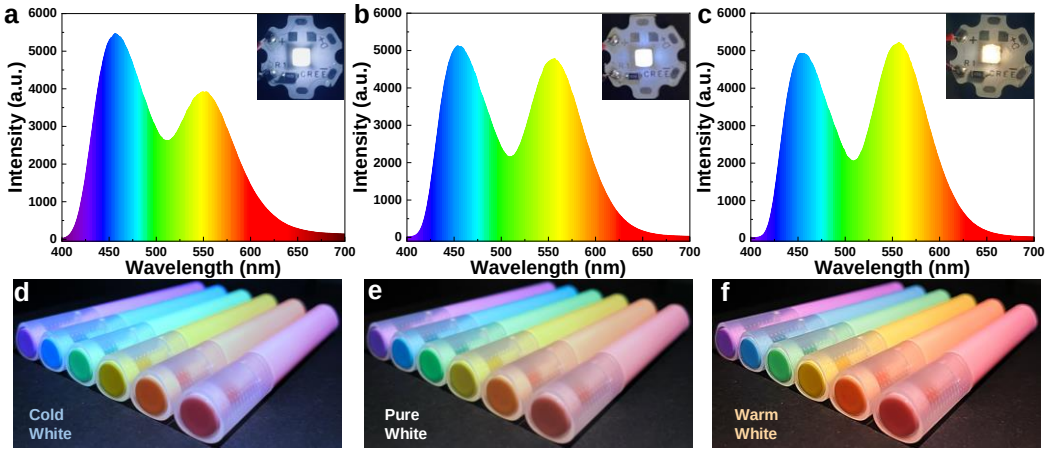

Fig. 6 (a-c) EL spectra of WLEDs fabricated with the $CsCaCl_3$:xMn^{2+} (x = 0.8%, 1%, 2%) on the 310 nm InGaN LED chip. (Inset: the device in a working state) (d-f) The color performances of paintbrushes under illumination by the WLEDs with different hues.

3.3. *Application in WLEDs with Different Hues*

We present the results obtained from the fabrication of WLEDs utilizing three distinct $CsCaCl_3$:xMn^{2+} phosphor crystals with varying Mn^{2+} concentrations (x = 0.8%, 1%, 2%) incorporated into a 310 nm InGaN LED chip. The electroluminescence (EL) spectra of these WLEDs, as shown in **Fig. 6**a-c reveal prominent broad emission bands attributed to the Mn^{2+} activator ions and STEs. The unique combination of these two emission features enables the generation of different hues of white light, facilitating the adjustment of color temperature. Specifically, we observe a tunable range from cool white to neutral white and warm white, providing versatility in white light output for various applications. Furthermore, as depicted in **Fig. 6**d-f, we assessed the color performance of objects under the illumination of the aforementioned WLEDs with distinct hues. Particularly, the paintbrushes exhibited differing color renderings when subjected to light from WLEDs with varying Mn^{2+} concentrations.

The increase in the working current from 10 mA to 100 mA results in a sequential rise in the intensity of the EL spectra of WLEDs fabricated with $CsCaCl_3$:xMn^{2+} (x = 0.8%, 1%, 2%) (**Fig. S9**). However, the shape of the emission peaks remains unchanged, indicating that the change in intensity is primarily due to an increase in the carrier injection and recombination rate. This observation underscores the stability of the emission color and composition of the WLEDs across a range of working currents, making them suitable for lighting applications.

4. Conclusions

In conclusion, our research has introduced a new class of luminescent crystals based on calcium halides, demonstrating their potential for various applications. The controlled doping of Mn^{2+} ions in $CsCaCl_3$ crystals resulted in tunable luminescent properties, ranging from broad blue emission to broad yellow emission, enabling the generation of diverse white light with adjustable color temperatures in WLEDs. The competitive charge distribution between Mn^{2+} and STEs was revealed, shedding light on the underlying luminescence mechanisms. The decomposition temperatures of 355 °C for $CsCaCl_3$ and 702 °C for $CsCaCl_3$:Mn^{2+}, highlight the role of Mn^{2+} doping in improving stability, which is supported by theory analysis. The response to the temperature of $CsCaCl_3$:Mn^{2+} STEs emission differed from that of Mn^{2+} emission, suggesting potential applications in temperature sensing. This study not only expands our understanding of luminescent materials but also provides practical insights for the development of novel solid-state lighting technologies.

Conflicts of interest

There are no conflicts to declare.

Acknowledgements

This research is financially supported by National Natural Science Foundation (NSF) of China (52172152), Key Projects of NSF of Zhejiang Province (LZ20E020003), and Doctoral Innovation Foundation of Wenzhou University.

References

1 F. W. Kang, G. H. Sun, P. Boutinaud, H. Y. Wu, F. X. Ma, J. Lu, J. L. Gan, H. D. Bian, F. Gao and S. Xiao, *Chem. Eng. J.*, 2021, **403**, 126099.
2 F. W. Kang, Y. P.Du, Z. Yang, P. Boutinaud, M. Wubs, J. Xu, H. Y. Ou, D. Z. Li, K. B. Zheng, A. T. Tarekegne, G. Sun, X. Xu and S. Xiao, *Laser Photonics Rev.*, 2022, **17**, 2200166.
3 Y. Q. Sun, L. S. Ge, L. J. Dai, C. Cho, J. F. Orri, K. Y. Ji, S. J. Zelewski, Y. Liu, A. J. Mirabelli, Y. C. Zhang, J. Y. Huang, Y. S. Wang, K. Gong, M. C. Lai, L. Zhang, D. Yang, J. D. Lin, E. M. Tennyson, C. Ducati, S. D. Stranks, L. S. Cui and N. C. Greenham, *Nature*, 2023, **615**, 830-835.
4 Y. Liu, S. P. Yan, T. C. Wang, Q. S. He, X. D. Zhu, C. Wang, D. Y. Liu, T. Wang, X.H. Xu and X. Yu, *Angew. Chem. Int. Ed.*, 2023, **62**, e202308420.
5 J. J. Luo, X. M. Wang, S. R. Li, J. Liu, Y. M. Guo, G. D. Niu, L. Yao, Y. H. Fu, L. Gao, Q. S. Dong, C. Y. Zhao, M. Y. Leng, F. S. Ma, W. X. Liang, L. D. Wang, S. Y. Jin, J. B. Han, L. J. Zhang, J.

Etheridge, J. B. Wang, Y. F. Yan, E. H. Sargent and J. Tang, *Nature*, 2018, **563**, 541-545.
6 Y. Q. Zhang, D. Tu, L. P. Wang, C. L. Li, Y. H. Liu and X. Y. Chen, *Mater. Chem. Front.*, 2023, DOI: 10.1039/d3qm00691c.
7 J. S. Yao, J. Ge, B. N. Han, K. H. Wang, H. B. Yao, H. L. Yu, J. H. Li, B. S. Zhu, J. Z. Song, C. Chen, Q. Zhang, H. B. Zeng, Y. Luo and S. H. Yu, *J. Am. Chem. Soc.*, 2018, **140**, 3626-3634.
8 H. Huang, R. F. Li, S. L. Jin, Z. F. Li, P. Huang, J. Q. Hong, S. W. Du, W. Zheng, X. Y. Chen and D. Q. Chen, *ACS Appl. Mater. Inter.*, 2021, **13**, 34561-34571.
9 M. L. Liu, N. Z. Jiang, H. Huang, J. D. Lin, F. Huang, Y. P. Zheng and D. Q. Chen, *Chem. Eng. J.*, 2021, **413**, 127547.
10 P. J. Song, B. Qiao, D. D. Song, J. Y. Cao, Z. H. Shen, Z. Xu, S. L. Zhao, S. Wageh and A. Al-Ghamdi, *ACS Appl. Mater. Inter.*, 2020, **12**, 30711-30719.
11 J. Guo, Y. H. Fu, M. Lu, X. Y. Zhang, S. V. Kershaw, J. Zhang, S. L. Luo, Y. X. Li, W. W. Yu, A. L. Rogach, L. J. Zhang and X. Bai, *Adv. Sci.*, 2020, **7**, 2000930.
12 M. Imran, J. Ramade, F. Di Stasio, M. De Franco, J. Buha, S. Van Aert, L. Goldoni, S. Lauciello, M. Prato, I. Infante, S. Bals and L. Manna, *Chem. Mater.*, 2020, **32**, 10641-10652.
13 H. P. Xu, W. Q. Liang, Z. Z. Zhang, C. Cao, W. S. Yang, H. M. Zeng, Z. E. Lin, D. W. Zhao and G. H. Zou, *Adv Mater*, 2023, **35**, e2300136.
14 Z. Tang, R. Z. Liu, J. S. Chen, D. Y. Zheng, P. W. Zhou, S. P. Liu, T. X. Bai, K. B. Zheng, K. L. Han and B. Yang, *Angew. Chem. Int. Ed.*, 2022, **61**, e202210975.
15 T. X. Bai, B. Yang, J. S. Chen, D. Y. Zheng, Z. Tang, X. C. Wang, Y. Zhao, R. F. Lu and K. L. Han, *Adv. Mater.*, 2021, **33**, 2007215.
16 P. Dang, G. Zhang, W. Yang, H. Lian, G. Li and J. Lin, *Chem. Mater.*, 2023, **35**, 1640-1650.
17 X. Q. Zhou, K. Han, Y. X. Wang, J. C. Jin, S. D. Jiang, Q. Y. Zhang and Z. G. Xia, *Adv. Mater.*, 2023, **35**, 2212022.
18 M. Gao, Y. X. Pan, C. D. Peng, Y. H. Ding, H. Z. Lian, L. Y. Li and J. Lin, *Chem. Mater.*, 2023, **35**, 773-782.
19 G. K. Dai, Z. M. Ma, Y. X. Qiu and Z. Y. Ma, *Inorg. Chem.*, 2023, **62**, 7906-7913.
20 B. Zhou, A. X. Du, D. Ding, Z. X. Liu, Y. Wang, H. Z. Zhong, H. N. Li, H. L. Hu and Y. M. Shi, *Nano-Micro Lett.*, 2023, **15**, DOI: 10.1007/s40820-023-01168-5.
21 Z. B. Liu, X. Z. Ji, Z. Z. Ma, F. Zhang, X. F. Qi, X. Chen, D. Wu, Y. Liu, M. C. Jia, X. J. Li, Y. Zhang, C. X. Shan and Z. F. Shi, *Laser Photonics Rev.*, 2023, **17**, 2300094.
22 S. X. Yang, C. H. Bi and J. J. Tian, *J. Phys. Chem. C*, 2021, **125**, 18810-18816.
23 S. S. He, Q. P. Qiang, T. C. Lang, M. S. Cai, T. Han, H. J. You, L. L. Peng, S. X. Cao, B. T. Liu, X. L. Jing and B. Jia, *Angew. Chem. Int. Ed.*, 2022, **61**, e202208937.
24 S. G. Ge, H. Peng, Q. L. Wei, X. D. Shen, W. G. Huang, W. Z. Liang, J. L. Zhao and B. S. Zou, *Adv. Opt. Mater.*, 2023, **11**, 2300323.
25 V. I. Anisimov, J. Zaanen and O. K. Andersen, *Phys. Rev. B*, 1991, **44**, 943-954.
26 Z. W. Lu, S. Chen, Y. F. Liu, C. X. Yuan, R. Y. Li, P. Sun, Z. H. Luo, Z. H. Liu and J. Jiang, *J. Alloys Compd.*, 2023, **956**, 170311.
27 X. Li, S. Q. Chen, P. F. Liu, Y. L. Zhang, Y. Chen, H. L. Wang, H. M. Yuan and S. H. Feng, *J. Am. Chem. Soc.*, 2020, **142**, 3316-3320.
28 D. Y. Li, J. H. Song, Y. Cheng, X. M. Wu, Y. Y. Wang, C. J. Sun, C. Y. Yue and X. W. Lei, *Angew. Chem. Int. Ed.*, 2022, **61**, e202206437.
29 J. C. Jin, Y. H. Peng, Y. T. Xu, K. Han, A. R. Zhang, X. B. Yang and Z. G. Xia, *Chem. Mater.*, 2022, **34**, 5717-5725.
30 A. Scrimshire, A. Lobera, A. M. T. Bell, A. H. Jones, I. Sterianou, S. D. Forder and P. A. Bingham, *J. Phys. Condens. Matter.*, 2018, **30**, 105704.
31 D. Y. Li, J. H. Song, Z. Y. Xu, Y. J. Gao, X. Yin, Y. H. Hou, L. J. Feng, C. Y. Yue, H. Fei, and X. W. Lei, *Chem. Mater.*, 2022, **34**, 6985-6995.
32 H. Peng and B. Zou, *J. Phys. Chem. Lett.*, 2022, **13**, 1752-1764.
33 Z. W. Jia, C. X. Yuan, Y. F. Liu, X. J. Wang, P. Sun, L. Wang, H. C. Jiang and J. Jiang, *Light Sci. Appl.*, 2020, **9**, 86.
34 J. Xue, Z. Yu, H. M. Noh, B. R. Lee, B. C. Choi, S. H. Park, J. H. Jeong, P. Du and M. Song, *Chem. Eng. J.*, 2021, **415**, 128977.
35 X. Li, D. D. Wang, Y. Zhong, F. Jiang, D. Q. Zhao, S. Q. Sun, P. Lu, M. Lu, Z. Y. Wang, Z. N. Wu, Y. B. Gao, Y. Zhang, W. W. Yu and X. Bai, *Adv. Sci.*, 2023, **10**, 2207571.
36 Z. J. Wu, L. Li, G. Tian, Y. J. Wang, F. L. Ling, Z. M. Cao, S. Jiang, G. T. Xiang, Y. H. Li and X. J. Zhou, *Dalton Trans.*, 2021, **50**, 11412-11421.
37 A. Q. Zhang, Z. Sun, M. C. Jia, Z. L. Fu, B. C. Choi, J. H. Jeong and S. H. Park, *J. Alloys Compd.*, 2021, **889**, 161671.
38 M. M. Shang, C. X. Li and J. Lin, *Chem. Soc. Rev.*, 2014, **43**, 1372-1386.